Plasma Physics and Controlled Fusion

PAPER

OPEN ACCESS

RECEIVED
28 January 2026

REVISED
7 April 2026

ACCEPTED FOR PUBLICATION
26 July 2026

PUBLISHED
14 August 2026

Design of DIVO: a diagnostic system for the ion velocity distribution function in fusion devices

S Molisani[1,2,*], G Nicolaou[3], D Verscharen[3], M Zuin[1,4], D Abate[1], A Belpane[1], M Giacomin[1,5], C Owen[3], O Pezzi[6], A Pimazzoni[1], I Predebon[1,4], F Pucci[6], L Sorriso-Valvo[6,7] and N Vianello[1,4]

1 Consorzio RFX (CNR, ENEA, INFN, Università di Padova, Acciaierie Venete SpA), Corso Stati Uniti 4, 35127 Padova, Italy
2 Centro Ricerche Fusione, University of Padova, Padova, Italy
3 Department of Space and Climate Physics, Mullard Space Science Laboratory, University College London, Dorking RH56NT, United Kingdom
4 Istituto per la Scienza e la Tecnologia dei Plasmi ISTP CNR, Padova, Italy
5 Dipartimento di Fisica "G. Galilei", University of Padova, Padova, Italy
6 Istituto per la Scienza e la Tecnologia dei Plasmi ISTP CNR, Bari, Italy
7 Space and Plasma Physics, School of Electrical Engineering and Computer Science, KTH, Stockholm, Sweden
* Author to whom any correspondence should be addressed.

E-mail: sara.molisani@igi.cnr.it

Keywords: diagnostic design, velocity distribution function, magnetized plasmas, ion detection, RFX-mod2

Abstract

In magnetized plasmas, many dynamical processes affect the ion velocity distribution function, both in laboratory and astrophysical environments. Measurements of this quantity can give useful insights for the study of phenomena such as magnetic reconnection, ion heating and acceleration, and turbulence. For this purpose, we designed a new diagnostic system that evaluates the ion velocity distribution function at the edge of fusion plasmas. The proposed device, called DIVO (Diagnostic for Ion Velocity Observation), resolves the two components of the ion velocity, parallel and perpendicular to the magnetic field. DIVO will be mounted at the plasma edge in the RFX-mod2 experiment, a Reversed-Field Pinch device, that has been upgraded for operation in 2026. DIVO offers a direct and local measurement that will enhance our knowledge on the thermal and supra-thermal ion populations at the plasma edge, as RFX-mod was not equipped with any instrument able to evaluate locally the ion distribution functions in velocity space. The working principle of this diagnostic system is based on the force balance between the electric and the Lorentz force, with the aim of interrupting the Larmor gyration of the ions, which is associated with the velocity component perpendicular to the magnetic field. Since the balance depends on the ion's perpendicular velocity, a specific externally applied electric field allows for the selection of ions with $v_\perp$ within a given range, while $v_{||}$ is evaluated by the ion's impinging position on a matrix of detectors. The instrument is equipped with a series of parallel thin metallic plates that filter the incoming ions, improving the resolution of the system. Individual particle simulations using Boris algorithm have been performed to optimize the instrument design and performances, assess its expected velocity resolution and operational range, and evaluate the transmission function needed to convert the detected counts into the original distribution function of the ions.

1. Introduction

In magnetized plasmas, both in laboratory and astrophysical environments, the knowledge of the ion velocity distribution functions (VDFs) is fundamental to understand plasma dynamics and in particular the relation between particle kinetics and plasma stability. Especially, some dynamical processes have been observed to strongly affect ion temperature and the ion velocity distribution function. One of the main examples are magnetic reconnection processes. Magnetic reconnection is a change in the topology of a set of field lines, which leads to a new equilibrium with lower magnetic energy [1]. This is a fundamental plasma physics phenomenon that has a multi-scale character, as it couples global MHD evolution and instability dynamics (e.g. magnetic shear and large-scale flows) with local micro physics such as kinetic effects and electron and ion dynamics [1–3]. The nature of dissipation in collisionless plasmas and the mechanisms governing the conversion of magnetic energy into particle heating and acceleration are directly rooted in the kinetic behaviour of electrons and ions, making the evolution of their velocity distribution functions central to resolve these major open questions in magnetic reconnection [4]. In space plasmas, reconnection is a key mechanism involved in several processes such as solar coronal heating [1, 5, 6], solar flares [7], substorms, and auroral events [8]. Moreover, magnetic reconnection generates plasma bulk flows, thermal and non-thermal particle populations through the acceleration of particles or thermalization of the plasma. For instance, ion energization in magnetic reconnection exhaust regions has been observed by Solar Orbiter [9]. Another mechanism that has been associated with particle energization in space plasmas is large-scale turbulence [10, 11]. Associated structures, such as flux ropes, magnetic islands, and plasmoids, lead to particle transport and acceleration [12–15].

Magnetic reconnection is a frequent process also in fusion relevant magnetically confined plasmas; in tokamaks, it causes sawtooth oscillations [16–18], while in reversed-field pinch (RFP) plasmas magnetic reconnection plays a fundamental role in the self-organization process that sustains the configuration [19, 20]. In the latter, magnetic reconnection is associated with rapid reorganization of the magnetic topology, the generation of magnetic flux (the so-called dynamo effect [21]), and the conversion of significant part of the magnetic energy into electron and ion acceleration and heating [22–25].

A precise information on the ion VDF can give useful insights for the study of these phenomena, both in laboratory and astrophysical plasmas. Many instruments and diagnostics have been developed for the purpose of investigating the ion energy and distributions. Space plasmas are routinely probed by in-situ particle instruments that reconstruct ion and electron velocity distribution functions under different environmental conditions [26]. These systems employ a variety of diagnostic techniques to study kinetic plasma processes throughout the Solar System. For instance, on missions such as MMS [27] and Solar Orbiter [28], dedicated plasma analyzers acquire full 3D ion and electron VDFs by combining electrostatic energy selection with nearly complete angular coverage, allowing high-resolution measurements of kinetic processes in the Earth's magnetosphere and the solar wind, respectively. Moreover, electrostatic analyzers combined with time-of-flight mass spectrometers are used on missions such as Cassini [29], Solar Orbiter [30], and Juno [31] to obtain species-resolved directional particle fluxes.

In present-day fusion devices, dedicated diagnostic systems are used to retrieve information on charged particle velocity distribution functions [32]. Fast ion losses induced by MHD activity can be measured by fast-ion loss detectors (FILD). These detectors—either scintillator-based [33] or Faraday-cup arrays [34] — directly measure the energies and pitch-angles of escaping ions. The fast ions are dispersed onto the detector plate with strike points that depend on their gyro-radius and pitch angle. Collective Thomson scattering (CTS) allows to probe confined fast ions in burning plasmas, via transverse laser probes. This system can provide temporally resolved and spatially localized measurements of the ion velocity distribution into the hundreds of keV-MeV range [35, 36]. Moreover, there are two diagnostics based on charge-exchange reactions between fast ions and injected neutrals. Fast Ion D-α spectroscopy (FIDA) gives information on the ion velocity distribution from the Doppler shift and broadening of the Balmer-α line emitted by the neutralized deuterium [32]. Neutral particle analysers (NPAs) detect the flux of fast neutrals that are generated via charge-exchange and measure their distribution function, which reflects those of the original fast ions, enabling the indirect determination of the ion temperature [32]. The NPA measurements are complementary to those of neutrons detectors, as they both detect ion distributions characterized by high energy tails. For instance, the time traces of neutron detectors clearly indicate ion acceleration during reconnection events in RFP plasmas, as they measure higher counts than expected when considering the core temperature, meaning that a supra-thermal ion population is locally present. The NPAs show a Maxwellian bulk population with an additional high energy tail that is consistent with ion heating due to reconnection [37].

In this paper, we propose a new diagnostic system to measure the ion velocity distribution function at the edge of fusion plasmas. The proposed device, called DIVO (Diagnostic for Ion Velocity Observation), resolves the two components of the ion velocity, parallel and perpendicular to the magnetic field. A direct and local measurement of the ion velocity distribution functions offered by DIVO will be complementary to the information given by NPA and neutron detectors. This paper focuses on the design of the proposed diagnostic system and the numerical simulations whose results have been used to optimize the instrument. The simulations shown in this paper take into account only the dynamics of a population of a single ion species, without considering the possible presence of electrons and neutrals. The work, therefore, disregards collisions, scattering, and collective effects. These phenomena need to be accounted for with dedicated end-to-end simulations that will be carried out in the second step of this project, as presented for example by [38]. The simulated parameters correspond to the environment of the RFX-mod2 experiment [39], a toroidal machine that can be operated both as a RFP and as a tokamak. It is the upgraded version of RFX-mod and is scheduled to start operation in 2026. The modifications implemented in the machine allow to enlarge the operational range to various magnetic configurations and plasma phenomena. Moreover, important improvements are under development in the diagnostics sector; some diagnostic systems have been upgraded, while others have been added [40].

DIVO is proposed to enhance our knowledge on the ions velocity at the plasma edge. This is an important improvement for the understanding of phenomena associated with thermal and supra-thermal ion populations that characterize RFP plasmas. One of the advantages of a RFP machine is its ability to maintain its plasma purely via Ohmic heating. It has been shown that a self-organized helical equilibrium characterized by improved confinement and strong transport barriers can be achieved with no additional plasma heating [41]. As there are no external heating systems that perturb the velocity of the particles, the observed features of the distribution functions are inherently associated to physical phenomena happening in the plasma, such as strong turbulence activity at the plasma edge. Being able to resolve the velocity distribution cast a light on specific properties of such effects. In RFX-mod spectroscopic measurements, exploiting Doppler shift effect, coupled with transport codes, were used to evaluate the flow of different ion species, also at the plasma edge [42]. Nevertheless, RFX-mod was not equipped with any instrument able to evaluate the ion distribution function in velocity space, as offered by DIVO.

The paper is structured as follows: section 2 illustrates the working principle, while in section 3 a baseline design of DIVO for RFX-mod2 is presented. Section 4 is dedicated to the numerical simulations used to optimize the instrument design and performances. This includes a discussion on the expected velocity resolution. In section 5, a comparison between the analytic and simulated uncertainties on the velocities is shown, while in section 6 the procedure to compute the geometric factor of the instrument is discussed and used to reconstruct an example of a synthetic Maxwellian distribution. Finally, in section 7 a brief summary and remarks conclude the paper.

2. Working principle

The ion population is gyrotropic, thus its distribution function is symmetric in the gyro-phase and depends only on the parallel $v_{\|}$ and perpendicular $v_{\perp}$ components of the velocity with respect to the magnetic field. These two components are evaluated simultaneously by DIVO. The working principle is based on the force balance between the electric and the Lorentz force, with the aim of interrupting the Larmor gyration of the ions, which is associated to $v_{\perp}$. The Larmor radius r_{L} of a particle of mass m and charge q in a magnetic field B can be expressed as:

$$r_{\mathrm{L}} = \frac{m v_{\perp}}{qB} \, . \tag{1}$$

In DIVO, the ions are subject to the existing B field inside the torus that enters the diagnostic system, plus an electric field, perpendicular to the B field, that is applied inside the device. In such conditions, the motion of a generic ion of mass m and charge q is governed by:

$$m \frac{\mathrm{d}\vec{v}}{\mathrm{d}t} = q\left(\vec{E} + \vec{v} \times \vec{B}\right). \tag{2}$$

To discuss in more details the motion of the ions, let us introduce a coordinate system such that x is the direction parallel to $\vec{B}$, y is perpendicular to both $\vec{E}$ and $\vec{B}$, and z is then the direction of $\vec{E}$, as indicated in figure 1, showing a CAD drawing of DIVO. By applying the electric field $\vec{E}$, the trajectory of the particles is modified. The magnitude of $\vec{E}$ can be chosen such that the right-hand side of equation (2) is equal to zero: no net force is acting on the particle, and it travels straight inside the device until it impinges on the detectors. This specific value of the electric field depends on the local B field and the component of the velocity that is perpendicular to both E and B fields:

$$E_z = v_y B_x. \tag{3}$$

The $v_{\perp}$ component is decomposed into $v_y = v_{\perp}\cos\theta$ and $v_z = v_{\perp}\sin\theta$, where θ is the gyro-phase angle at the aperture. If a particle has $v_{\perp}$ and the entrance phase θ satisfying equation (3) then it does not gyrate during its passage through DIVO, its velocity is constant, and its motion is in the plane perpendicular to $\vec{E}$ (xy). For $v_{\perp}$ and θ not matching equation (3), the particles experience the force due to the

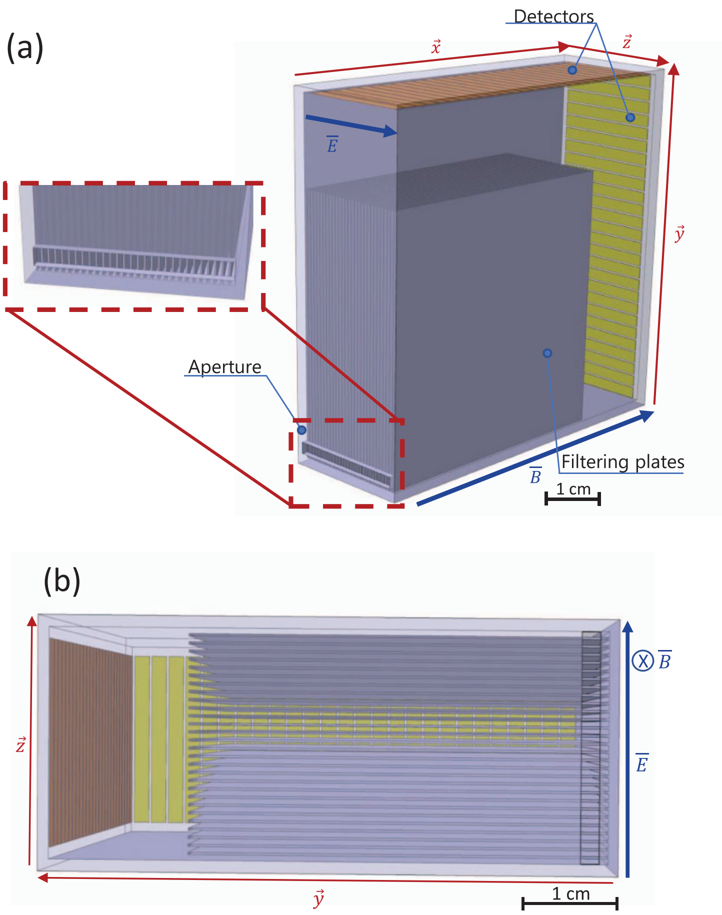

Figure 1. CAD drawings of DIVO: (a) highlights of the main components, (b) *yz* view. The coordinate system and the direction of the simulated fields are shown with red and blue arrows, respectively. The detecting screens are shown in orange and yellow.

E and B fields, they oscillate and drift for $\vec{E}\times\vec{B}$. The equations of motion can be derived starting from equation (2):

$$\begin{cases} \dot{v}_x = 0 \\ \dot{v}_y = \frac{q}{m} v_z B_x \\ \dot{v}_z = \frac{q}{m}\left(E_z - v_y B_x\right) \quad , \end{cases} \tag{4}$$

taking the derivative and substituting:

$$\begin{cases} \ddot{v}_x = 0 \\ \ddot{v}_y = -\omega^2 v_y + \omega^2 \frac{E_z}{B_x} \\ \ddot{v}_z = -\omega^2 v_z \ , \end{cases} \tag{5}$$

where $\omega = \frac{q}{m} B_x$ is the Larmor pulsation. These equations describe a harmonic oscillator in velocity and position and their solution gives the positions and velocities as a function of time:

$$\begin{cases} x(t) = v_x t \\ y(t) = \frac{A_y}{\omega}\sin(\omega t) + \frac{E_z}{B_x} t \\ z(t) = \frac{A_z}{\omega}\sin(\omega t) \end{cases} \tag{6}$$

$$\begin{cases} v_x(t) = const \\ v_y(t) = A_y \cos(\omega t) + \frac{E_z}{B_x} \\ v_z(t) = A_z \cos(\omega t) \quad , \end{cases} \tag{7}$$

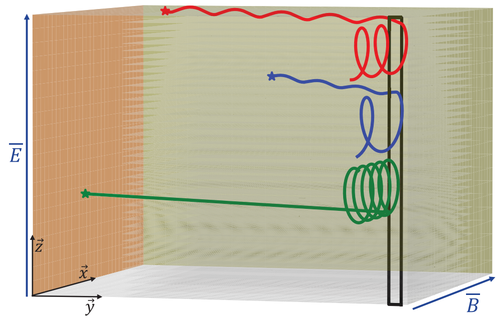

Figure 2. 3D trajectories of three particles with different values of $v_{||}$, $v_\perp$ and θ. The ions gyrate outside DIVO, then enter through the aperture (shown in black) and drift and oscillate between the filtering plates (shown in grey). They impinge on the detectors (indicated by star markers).

with the amplitudes $A_y = v_\perp \cos\theta - \frac{E_z}{B_x}$ and $A_z = v_\perp \sin\theta$. The motion in x is unperturbed by the fields, while the trajectory in y and z is characterized by oscillation and drift. Figure 2 shows the trajectories of three test particles in DIVO. They are all simulated with random $v_{||}$, $v_\perp$ and θ. In particular, the green particle simply drifts inside the instrument because it has $v_\perp$, θ at the aperture satisfying equation (3); the same is not valid for the red and blue particles, that therefore drift and oscillate.

The described motion inside the device is interrupted when the ions reach either of two detecting screens placed on the rear faces of DIVO, indicated in orange and yellow in figures 1 and 2. Using the detectors, the ions' velocity is evaluated as follows:

As regards the perpendicular component of the velocity, all the particles that are detected in a certain time interval in which the applied E field is fixed, are assumed to have $v_\perp$ that satisfies equation (3), with a certain resolution. This resolution is computed starting from the range of velocities of the detected particles around this $v_\perp$ value, as explained in more details in section 4.2.1. If no collimating system is present, almost the totality of the particles entering the aperture will arrive at the detectors, even those that are oscillating with a velocity quite different from $v_\perp$. To make sure that only those particles with a perpendicular velocity within the range around $v_\perp$ are detected, a filtering system is needed. For this purpose, the instrument is equipped with a series of parallel thin metallic plates in the xy plane, shown in figure 1 in grey. The gap between two consecutive plates is such that the particles whose gyration is not interrupted hit these plates and do not reach the detectors. This filtering method is a key element of the device, as it allows to select the correct $v_\perp$-θ particles and improve the resolution of the system. During operation, the potential difference across the device, that defines E_z, is varied in order to scan the distribution in $v_\perp$.

In the direction parallel to the magnetic field, the velocity component v_x of the particles is not affected by the fields and stays constant inside the device. The arrival position of the ions on the detecting screens is related to this component of the velocity. Since the final position x_f of the ions depends on the total velocity, the relationship between x_f and the value of the parallel velocity changes with the perpendicular one. Analytic calculations and simulation results are used to map the position on the screens with the value of the parallel velocity for all possible values of $v_\perp$. In section 4 we expand on this aspect.

3. Design of the system

Figure 1 shows the baseline design for DIVO. The proposed diagnostic system has the shape of a rectangular cuboid of dimensions ≈6×6×2 cm. It is composed by the following main components: a thin aperture, two detecting screens, two electrodes, and a series of filtering plates.

The aperture, whose width is around 2 mm, must be placed in the plane perpendicular to the direction of the local magnetic field to ease the entrance of the ions that are travelling following the field lines. In the RFP configuration, the magnetic field at the plasma edge is mainly poloidal, with a much smaller toroidal component, which can be considered as a minor correction of the main B field. To orient DIVO correctly, it is important to know the direction of the magnetic field with a high enough time resolution; for this purpose local tri-axial Hall sensors are used.

To detect the ions, the two rear faces xz and yz are covered with arrays of miniaturized detectors. By adopting two detecting screens it is possible to sample the distribution in the velocity space with both $v_\perp$ and $v_\parallel$ positive, without losing any information, as it would happen by using only one screen. The individual detectors must be small to increase the number of bins and improve the spatial (and thus speed) resolution of the measurement. Since the expected incoming flux is large, we plan to adopt current-mode detectors such as Faraday cups (FC). Micromachined Faraday-cup arrays have been demonstrated using MEMS/DRIE fabrication techniques [43, 44], and micro-Faraday-cup matrices have been deployed in fusion experiments to measure low-energy plasma ions [45]. Micro-FC arrays guarantee fine per-pixel current measurements, but, in the energy range of our interest, require appropriate secondary-electron suppression and careful electrical isolation to maintain accuracy [43]. Moreover, the associated electronics must be capable of collecting a wide range of currents. If the further analysis of collective effects, for example those induced by space-charge phenomena, imposes the necessity to reduce the particle flux into the device, then our detecting scheme would be based on single-particle counting detectors. In this case, Microchannel plate-based arrays will be employed, though for the ion energy range of interest, post-acceleration or a conversion surface is generally required to maintain high detection efficiency [46–48].

The two electrodes are placed on the two faces parallel to the xy plane and produce a uniform electric field of the order of tens of $\mathrm{kV\,m^{-1}}$ across the device.

The metallic filtering plates are parallel to the electrodes, thus perpendicular to the aperture. The distance between the filtering plates, labelled as Δl, is a key parameter that has been optimized using simulations and has been fixed to 0.5 mm, as explained in section 4.2.3. Also the dimensions of the plates have been selected in order to minimize the metallic surface while ensuring that the ions complete at least one oscillation before the end of the plates, in a variety of plasma conditions.

For its use in RFX-mod2, DIVO will likely be mounted on the Fast Reciprocating Manipulator FaRM [49]. This is a new equipment of RFX-mod2 that allows for rapid insertion and retraction of diagnostic probes in the plasma. With a slow movement, the FaRM moves the diagnostic system close to the plasma edge, ready for the fast insertion deeper in the plasma. Thus, different locations of the plasma could be investigated. Alternatively, DIVO can be positioned at a fixed toroidal and poloidal position on the tiles of the first wall.

Plasma electrons would easily enter the aperture of DIVO as their Larmor radius is much smaller than the ion Larmor radius, filling the chamber and creating unwanted side effects, such as scattering on filtering plates, collisions, ionization of neutrals, and false current signals on the detectors. Therefore, we must prevent the electrons from entering the device. For this purpose, we propose a multi-grid structure that will be designed and optimized with dedicated simulations, and then integrated in front of DIVO, just outside the aperture. This system is likely to be composed of a first electron repeller grid, biased with a negative potential relative to the plasma to repel plasma electrons, and then a set of electrostatic lenses to compensate the optics of the extracted positive ions. This system and the above mentioned triaxial Hall sensors are among the additional modular units required to support the correct operation of DIVO. However, the design of these parts is beyond the scope of this paper, as our current focus lies on the study of the feasibility of the fundamental measurement concept and the expected preliminary performance of the diagnostic for the VDF of a population of single ions.

4. Numerical simulation

Individual particle simulations have been carried out to simulate the trajectories of the ions in a region of applied electric and magnetic fields within the geometry of the device. Given the need to resolve the full particles' gyration, we choose to use the Boris algorithm [50] to push the particles and update their velocity and position.

4.1. Boris algorithm

The Boris algorithm is a quite commonly used numerical method in plasma physics and particle-in-cell (PIC) simulations for computing the motion of charged particles in electromagnetic fields. It uses an explicit and time-centered scheme and conserves phase-space volume [51]. It consists in separating the

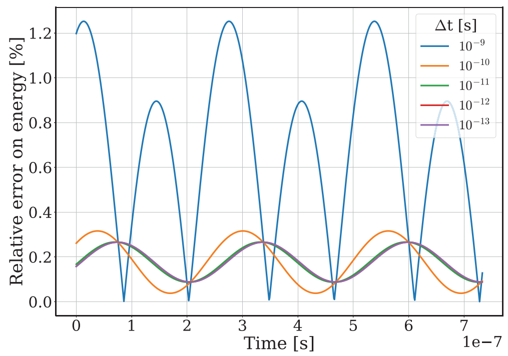

Figure 3. Relative error on the total energy of a test particle from simulations with different timesteps Δt. The largest relative error for $\Delta t = 10^{-9}$s is 1.25%.

effect of the fields in three steps: first half acceleration due to E field is computed, then the full rotation due to the B field, and finally the other half acceleration, as expressed in equation (8), discussed in [51–53].

$$\begin{cases} v^- = v^{n-1/2} + \frac{qE}{m}\frac{\Delta t}{2} \\ \frac{v^+ - v^-}{\Delta t} = \frac{q}{2m}\left(v^+ + v^-\right) \times B \\ v^{n+1/2} = v^+ + \frac{qE}{m}\frac{\Delta t}{2} \end{cases}, \tag{8}$$

where Δt is the timestep, $v^{n-1/2}$ and $v^{n+1/2}$ are the velocities at a $\mp$ half timestep, respectively, and v^-, v^+ are two intermediate states. The fields could be updated as well, but in these simulations we keep them uniform and constant. We fix E field by the potential difference we impose between the electrodes, while we assume that the flux of incoming particles does not affect the magnetic field.

In a constant magnetic field without electric field, the method has good long-term energy conservation. Instead, in presence of electric fields the total energy is not conserved and the error depends on Δt [51]. The choice of Δt is driven by a compromise between improving the accuracy, assuring the stability, and reducing the computational cost. Regarding the stability, the method is conditionally stable: stability depends on the Larmor gyration and it is good practice to choose Δt to be well below $\frac{2\pi}{\omega}$. As regards the accuracy, the Boris algorithm has a second order accuracy: we have checked with a test particle simulation that the truncation error in position and velocity scales as $(\Delta t)^2$ for Δt between 10^{-12}s and 10^{-9}s. Our code automatically selects the value of Δt as $\frac{0.035}{\omega}$ to reduce the error to less than 0.1%, according to [52]. Expressed in terms of angle of rotation, this corresponds roughly to 1/180 of the period. A typical value for Δt is therefore in the range $[7 \cdot 10^{-10}, 2 \cdot 10^{-9}]$s, depending on the gas species and the B field used in the simulation.

We verify that the error on the total energy is negligible for our cases as it is much smaller than the resolution, as shown in figure 3.

To do so, we run a test particle simulation and we observe how the energy changes at each time step with respect to its initial value. The initial energy has just the contribution of the kinetic energy, while the total energy during the motion inside the electric and magnetic fields is given by the kinetic and electrical potential energy. The maximum relative error on the total energy observed is 0.32% for $\Delta t = 10^{-10}$s and 1.25% when using $\Delta t = 10^{-9}$s. While it reduces with Δt, it does not depend on the initial conditions of the particle, e.g. its velocity. Moreover, we observe that the energy error does not increase with the number of timesteps, meaning it is globally bounded, property associated with the algorithm being volume-preserving, as discussed in [51].

4.2. Simulation output

We use the simulation outputs to optimize the design of the device, to define its operational range, to assess the resolution of the instrument, and to evaluate the transmission function needed to convert the detected counts into a measurement of the original distribution function of the ions.

Simulations are carried out for a range of typical plasma conditions, by considering different ion species and varying the magnetic field value. These two quantities strongly influence the value of the Larmor radius, and consequently the number of detected ions and the resolution vary significantly. The device performance is evaluated as a function of these parameters.

Table 1. Simulated plasma conditions.

Gas	B field (T)	r_L (mm)	$\vec{E}$ field (kV m^{-1})
D_2	0.3	2.1 – 7.5	10–32
D_2	0.5	1.3 – 4.6	15–55
D_2	0.8	0.8 – 2.9	25–83
H_2	0.5	0.6 – 2.3	16–55

Independent particles are initiated with random parallel $v_{||}$ and perpendicular $v_{\perp}$ velocities, uniformly distributed over a range spanning from 10 km s^{-1} to 120 km s^{-1}. Their initial gyrophase θ is random and uniform between 0 and 2π. Each simulation generates ions until 10^5 ions are counted on the detecting screens. Each simulation has a fixed value of the electric field E_z; therefore, in order to sample the perpendicular velocity distribution, many different simulations have to be run with the same plasma conditions and a different $\vec{E}$ field applied across the device. The same can be repeated changing the ion species and the magnetic field to simulate other possible plasmas. In particular, in this paper we report the case [gas $= D_2$, $B = 0.5$ T], as well as a comparison between the results of the four conditions listed in table 1.

4.2.1. Evaluation of $v_{\perp}$ resolution

For each simulation with a fixed electric field, we anticipate that the ions reaching the detectors have a $v_{\perp}$ around the theoretically expected value E_z/B_x, according to equation (3). Indeed, the results show that the detected perpendicular velocities of the ions are distributed according to a transmission curve with a Gaussian shape, that represents the statistical response of the detection to the input uniform velocity distribution.

The mean value of this transmission curve corresponds very closely to E_z/B_x. An example is shown in figure 4(a) for [gas $= D_2$, $B = 0.5$ T]: the detected $v_{\perp}$ are distributed around the value $= E_z/B_x =$ 53.6 km s^{-1}. With the Gaussian fit, we find a full width half maximum ($V_{\perp}^{\mathrm{FWHM}}$) ≈ 6.0 km s^{-1}.

Figure 4(b) shows the transmission curves of $v_{\perp}$ for 10 simulations at different values of electric field. With this choice of E field values, some curves overlap and others are well separated; it is preferable to have curves in continuity at half height, to guarantee a better sampling of the $v_{\perp}$ distribution. Therefore, it is a matter of optimizing the value of $\vec{E}$ to be applied during operations. In a generic case, this is done by fitting the data points of the $V_{\perp}^{\mathrm{FWHM}}$ versus the electric field, finding an analytic relation between the two quantities, and imposing that the distance between two values of the applied E field is equal to the sum of the halves of the corresponding $V_{\perp}^{\mathrm{FWHM}}$s. As shown in figure 5, all the transmission curves have a similar $V_{\perp}^{\mathrm{FWHM}}$, that does not depend on the applied electric field. Therefore, the values of $v_{\perp} = \frac{E_z}{B_x}$, and consequently of the optimized E_z, are simply separated by an averaged $V_{\perp}^{\mathrm{FWHM}}$.

Figure 4(c) shows the transmission curves of $v_{\perp}$ for the new values of electric field. These are the optimal values to be applied for this plasma condition to reconstruct the velocity distribution.

From the full width half maximum the resolution is determined as

$$v_{\mathrm{RES}}\,[\%] = \frac{V_{\perp}^{\mathrm{FWHM}} \cdot 100}{v_{\mathrm{mean}}}\,. \tag{9}$$

Clearly, a smaller $V_{\perp}^{\mathrm{FWHM}}$ means a more efficient filtering of the ions that reach the detectors, yielding better resolution. The perpendicular velocity resolution is shown in figure 6 for the four simulated plasma conditions.

As the resolution changes with $v_{\perp}$, mass, and magnetic field, it is strongly related to the Larmor radius of the ion. The filtering plates are more efficient at larger Larmor radii: this explains the trend of the resolution of the four conditions as well as with the velocity. The [gas $= H_2$,B $= 0.5$ T] condition is the one with the smallest r_L and indeed it shows the worst resolution, with a maximum around 37%. The resolution is related to the number of points used to sample the distribution function. The 15 selected values (shown in figure 4(c)) allow to sample the distribution with a resolution that is at most 19.4% (shown by the red dots in figure 6).

4.2.2. Evaluation of $v_{||}$ resolution

The parallel velocity is computed according to the position at which the ions impinge on the detecting screens. The z coordinate does not play a role in the evaluation of $v_{||}$. It is computed from the x coordinate for particles landing on the detecting screen in the xz plane, and from the y coordinate for particles landing on the detecting screen in the yz plane. The two screens are covered with small detectors and

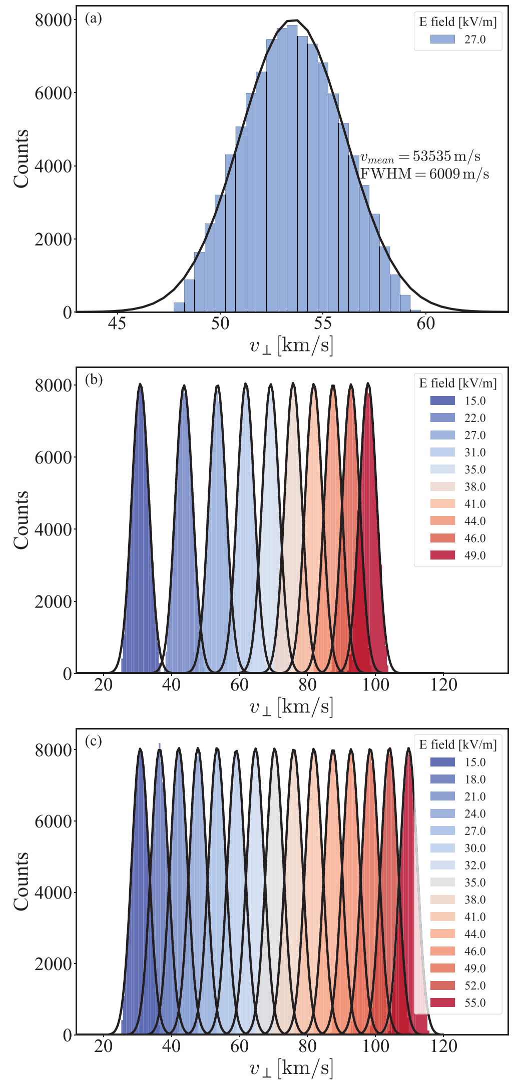

Figure 4. Fit of the $v_\perp$ transmission curves for the simulations of ions of D_2 at B = 0.5 T. (a) Histogram of the $v_\perp$ detected for the simulation with $E_z \approx 27$ kV m^{-1} and Gaussian fit; (b) Histograms and fits of 10 simulations applying 10 different values of the electric field; (c) Histograms and fits of simulations with the optimized $\vec{E}$ field.

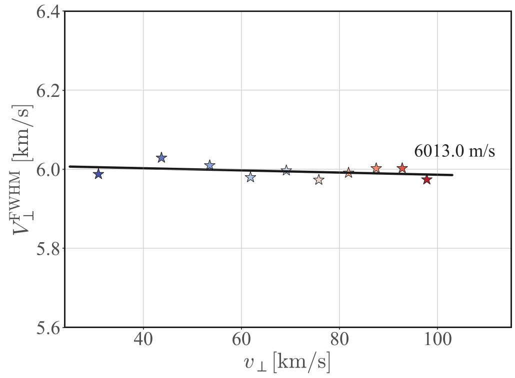

Figure 5. Full width half maximum of the Gaussian transmission curves of $v_\perp$ from the simulations in figure 4(b). The fit gives the average value of the $V_\perp^{\mathrm{FWHM}}$.

all the ions collected by the same detector, at a fixed E_z setting, are assumed to have the same parallel velocity. Therefore the resolution of this component is associated to the size and number of detectors. In the simulations, the detecting screens are divided in bins that represent the positions of the detectors along the relevant direction, i.e. each bin covers the entire z dimension. For each bin, whose width is Δx

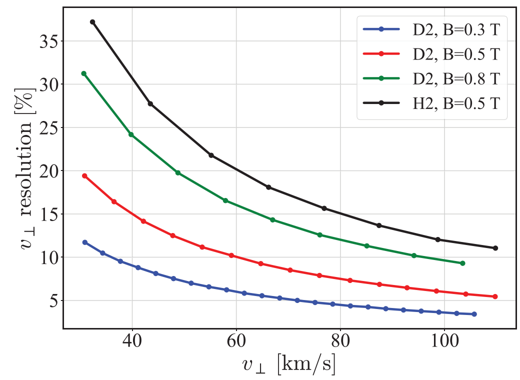

Figure 6. Comparison of the resolution in $v_\perp$ for four different plasma conditions.

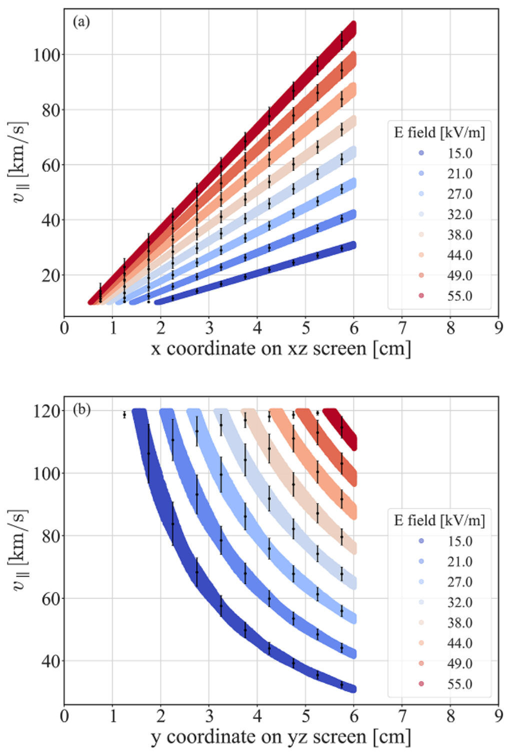

Figure 7. $v_\parallel$ for 8 simulations of D_2, B = 0.5 T each considering a different applied electric field. Each screen is divided in 12 bins of width $\Delta x = 0.5$ cm. The $v_\parallel$ mean and $V_\parallel^{\mathrm{FWHM}}$ is computed for each bin. (a) the *xz* screen shows a linear relationship between the $v_\parallel$ and the position along *x*, (b) the *yz* screen shows that $v_\parallel$ is inversely proportion to the position along *y*.

for both screens, the transmission curve of the detected parallel velocity $v_\parallel$ is considered. Figure 7 shows the curve's mean values with black dots and the $V_\parallel^{\mathrm{FWHM}}$ with error-bars. These are over-plotted on the coloured traces that represent all the 10^5 simulated ions' parallel velocities for each applied electric field. The case of 12 detectors with $\Delta x = 0.5$ cm for each detecting screen is shown. The relationship between position and parallel velocity is different depending on the orientation of the screen: for the *xz* screen, $v_\parallel$ is linear with x (figure 7(a)) while in the *yz* screen, $v_\parallel$ is inversely proportional to y (figure 7(b)).

Ions with the same $v_\parallel$ reach a different final position on the detecting screens, for different applied electric fields. Indeed, the travelled distance depends on both parallel and perpendicular velocities and the latter is defined, within a narrow range, by the value of E_z. For example, for the strongest E_z applied, almost all the simulated particles reach the *xz* screen. Clearly, this is also associated with the limited range of velocities that are simulated: we do not simulate particles with a velocity component larger than 120 km s^{-1}. We also see that the range of detected $v_\parallel$ spreads as $v_\parallel$ increases, yielding a larger $V_\parallel^{\mathrm{FWHM}}$.

Figure 8 shows the $v_\parallel$ resolution computed as the ratio between the $V_\parallel^{\mathrm{FWHM}}$ and $v_\parallel$ mean value, for the simulations of figure 7.

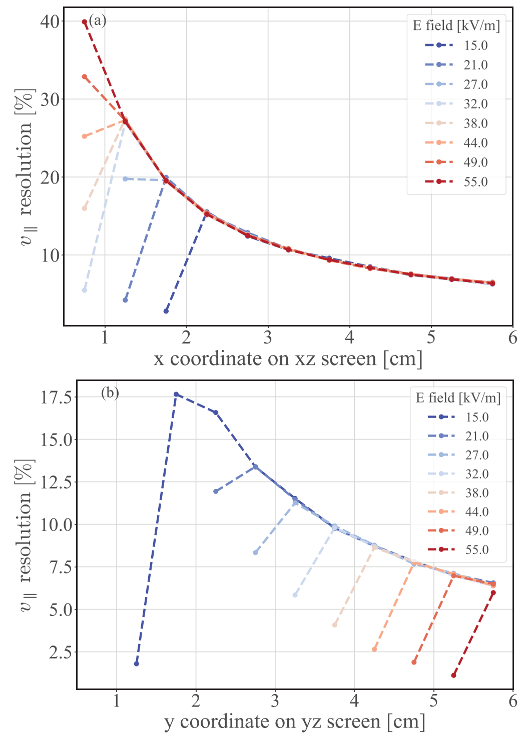

Figure 8. $v_{\parallel}$ resolution shown for (a) the *xz* screen and (b) the *yz* screen, for the same simulations and bins as figure 7.

The resolution of the bins in the *yz* screen is better than the one of the *xz* screen, and both show a resolution for the central bins always below 10%, while the external bins are characterized by a larger resolution, that in the case of the *xz* screen reaches a maximum value of 40%. For each simulation, the outermost populated bin—corresponding to the data point out of trend—typically exhibits a much better resolution. This is again related to the limited velocity range of the simulations, as few counts are detected in these bins. If the full range of velocities were sampled, the data points would align with the trend, that appears to be the same for all simulations, and carries the meaningful information on the resolution.

Moreover, the resolution does not depend on the plasma conditions, as shown in figures 9(a) and (b). The same detector is characterized by the same $v_{\parallel}$ resolution in any plasma condition. The resolution strongly depends on the size of the detectors. Figures 9(c) and (d) compare the trends of the $v_{\parallel}$ resolution at various sizes of the detectors Δx for the two screens. As expected, smaller detectors provide better resolution. However, the use of such small detectors could be challenging, as, for instance, a higher number of detectors would mean increasing the difficulty in managing the space available as well as the complexity of the analogue front-end. There is a trade-off between improving the resolution and the overall complexity of the device.

4.2.3. Choice of distance between filtering plates Δl

One of the key design parameters of the instrument is the distance between the filtering plates, Δl. This parameter must be chosen carefully based on the required velocity range and resolution. By choosing a small Δl, fewer particles with a residual gyration pass between two filtering plates, improving the resolution in $v_{\perp}$. However, this choice also reduces the flux of particles that reach the detecting screens, in particular for higher $v_{\perp}$. Moreover, the value of Δl is also limited by the technical complexity of the mechanical manufacturing process for such a layered structure. Determining the optimal value of Δl is therefore a trade-off between the filtering efficiency and resolution against the difficulty of manufacturing and assembling the instrument. We run various simulations using Δl as a free parameter under the plasma conditions listed in table 1, in order to quantify its effects on the $v_{\perp}$ resolution. We show the resulting $v_{\perp}$ resolution for four different values of Δl in the case [gas = D_2, B = 0.5 T] in figure 10.

We select $\Delta l = 0.5$ mm as optimal value for this baseline design and we fix it for all the simulations whose results are shown in this paper.

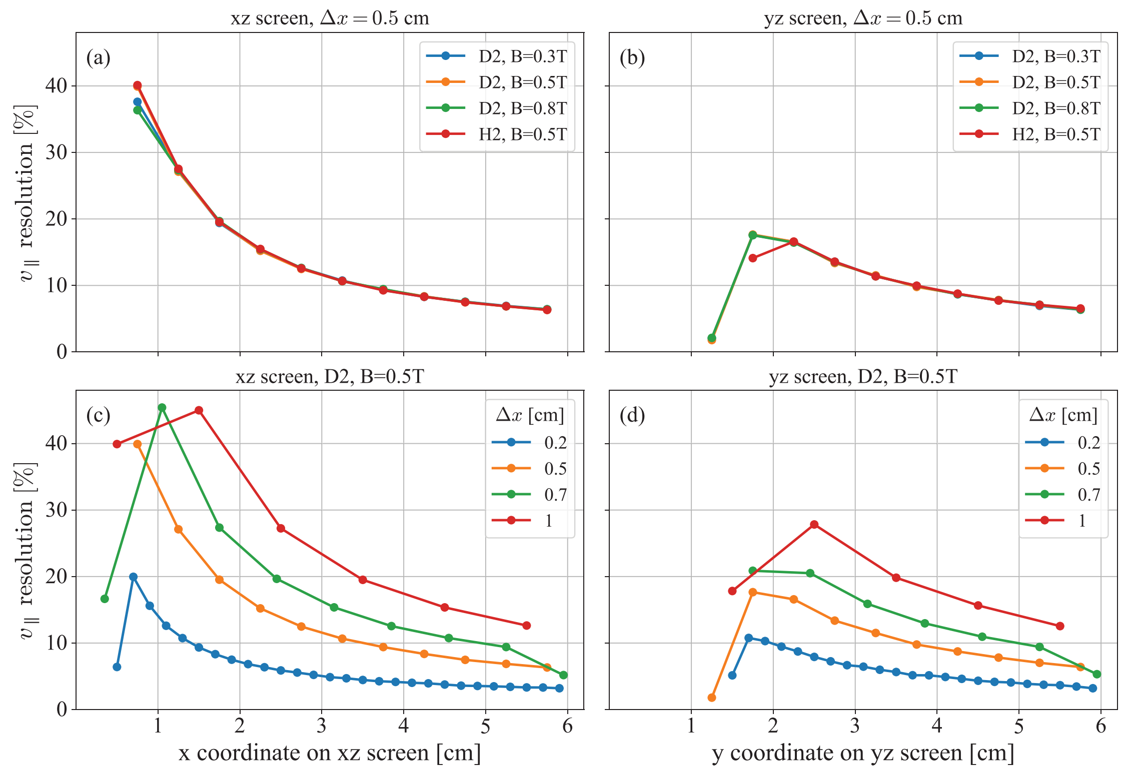

Figure 9. Comparison of the resolution in $v_\parallel$. (a) and (b): four different plasma conditions at a fixed bin width Δx for the two detecting screens. (c) and (d): four different Δx values for the $[D_2, B = 0.5\ \mathrm{T}]$ case for the two detecting screens.

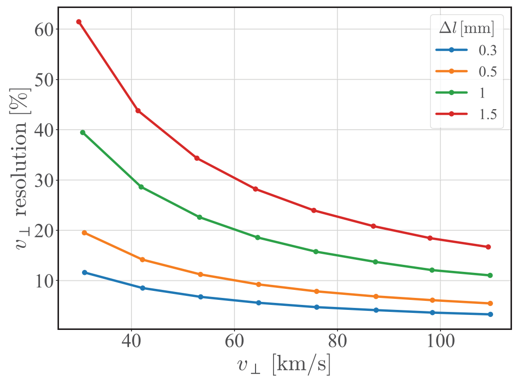

Figure 10. Range of the $v_\perp$ resolution for four values of the distance between the filtering plates Δl, in the case [gas = D_2, B = 0.5 T].

5. Comparison between simulation results and analytic relations

We analytically compute the motion of the ions inside the device with the equations reported in section 2. The motion is expressed in terms of three parameters: $\theta, v_\perp, v_\parallel$. Moreover, we derive the expressions of the associated uncertainties $\Delta\theta$, $\Delta v_\perp$, and $\Delta v_\parallel$. The analytic expressions of each term are then compared with the results of the simulations.

5.1. $\Delta\theta$ and $\Delta v_\perp$

The resolution in perpendicular component is associated to the range of velocities of the ions reaching the detecting screens. This is due to the fact that between two filtering plates there is space for the ions to travel even if they undergo some remnant gyro-motion. The oscillation can arise from the following effects: ions entering with $v_\perp$ that matches the condition of equation (3) ($v_\perp = \frac{E_z}{B_x}$) but an entrance phase different from zero (gives uncertainty $\Delta\theta$), or ions entering with a different perpendicular velocity at $\theta = 0°$ (gives uncertainty $\Delta v_\perp$), or the combination of these two.

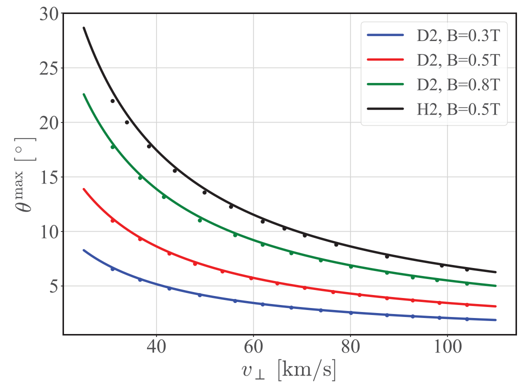

Figure 11. $\theta^{\max}$ for 4 different plasma conditions. The simulated outputs (dots) agree with the analytic expression (full line) of equation (11).

To compute the expressions of $\Delta\theta$ and $\Delta v_\perp$ analytically, we exploit the fact that the ions that oscillate in the z direction will reach the detecting screens only if they do not impact on the filtering plates, that are Δl apart.

For $\Delta\theta$, from equation (6), the amplitude of the gyration in the z direction is:

$$A_z = \frac{v_\perp \sin\theta}{\omega} = \frac{m}{qB_x} v_\perp \sin\theta \ . \tag{10}$$

Ions can transit between the plates if A_z is less than $\frac{\Delta l}{2}$, that corresponds to a maximum phase $\theta^{\max}$:

$$\theta^{\max} = \sin^{-1}\left(\frac{qB_x}{m}\frac{\Delta l}{2v_\perp}\right) \ . \tag{11}$$

Here, for simplicity, $\Delta\theta$ is defined as the difference between the smallest and the largest accepted angle:

$$\Delta\theta = 2\cdot\theta^{\max} \quad = \quad 2\sin^{-1}\left(\frac{qB_x}{m}\frac{\Delta l}{2v_\perp}\right) = 2\sin^{-1}\left(\frac{\Delta l}{2r_\mathrm{L}}\right) \ , \tag{12}$$

as the system is observed to be symmetric in accepted angle around the most probable value, $\theta = 0°$. As previously observed, particles with a small Larmor radius have a higher possibility to be detected, since a larger entrance phase is accepted.

For $\Delta v_\perp$, we consider $v_y = v_\perp$ and $v_z = 0$ and by using equations (4) and (7) we calculate the maximum amplitude in z direction:

$$\frac{A_z{}^{\max}}{\omega} = \Delta l = \frac{\frac{E_z}{B_x} - v_\perp}{\omega} \ . \tag{13}$$

The difference $\frac{E_z}{B_x} - v_\perp$ is $\Delta v_\perp$, which is then defined as:

$$\Delta v_\perp^{\max} = \omega \Delta l \ . \tag{14}$$

This expression does not depend on the perpendicular velocity itself, therefore it is constant for all $v_\perp$ for a given set of q, m, and B.

We compare the final expressions for $\Delta\theta$ (equation (12)) and $\Delta v_\perp$ (equation (14)) with the outputs of specific sets of simulations to check the agreement between theory and the numerical model. To verify the expression for $\Delta\theta$, we fix the initial perpendicular velocity of the simulated ions to $\frac{E_z}{B_x}$ with random v_y,v_z components; for $\Delta v_\perp$ the initial perpendicular velocity is random but the entrance phase is fixed at 0 ($v_y = v_\perp$,$v_z = 0$).

In figure 11, the dots show the results of our simulations in terms of $\theta^{\max}$, for various values of $v_\perp$ and the 4 different plasma parameters listed in table 1; the lines are the corresponding analytic relations, from equation (11). There is very good agreement between the simulation output and the analytic expression.

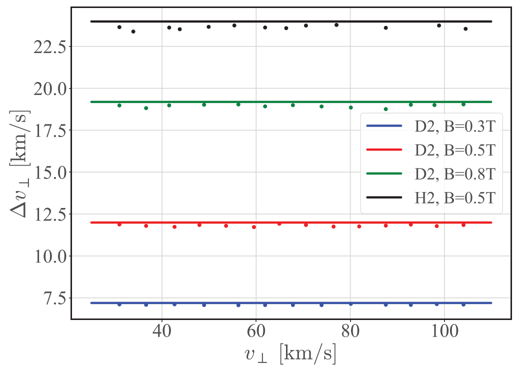

Figure 12. $\Delta v_\perp$ for 4 different plasma conditions. The simulated outputs (dots) agree with the analytic expression (solid line) of equation (14).

The simulated values, computed as the difference between the largest and the smallest detected $v_\perp$, and the analytic relation from equation (14) for $\Delta v_\perp$ are shown in figure 12. The relative error between the analytic and simulated $\Delta v_\perp$ is always below 2.5%. $\Delta v_\perp$ is comparable with the $v_\perp$ mean value, especially in the [H_2,0.5 T] case; for instance, for a $v_\perp \approx 30$ km s^{-1}, the associated $\Delta v_\perp$ is ≈ 24 km s^{-1}. Indeed, these values of $\Delta v_\perp$ are much larger than the $v_\perp$ resolution computed from the simulations output (shown in figure 6). This difference is due to the definition of $\Delta v_\perp$, that introduces a factor $\approx$ 2 with respect to the $V_\perp^{\mathrm{FWHM}}$ used in figure 6.

5.2. $\Delta v_{||}$

This term accounts for the range of parallel velocities that are detected in the same detector. In the simulations, each detector is represented by its Δx. In the analytic calculations, the same quantity is labelled as $\mathrm{d}x_d$ for the xz screen and $\mathrm{d}y_d$ for the yz screen. These are the uncertainties due to the dimension of the detector. Moreover, the size of the aperture in the y direction, dy_a, is another source of uncertainty, as the y position of the ions at the aperture is unknown within this range. From the equation of motion of the particles in the xy plane:

$$\begin{cases} x(t) = v_x t \\ y(t) = \frac{E_z}{B_x} t \end{cases}, \tag{15}$$

neglecting any remnant oscillation, as only the case with $v_\perp = \frac{E_z}{B_x}$ is considered. This leads to:

$$v_{||} = \frac{E_z}{B_x} \frac{x}{y} . \tag{16}$$

The parallel velocity is directly proportional to the x position and inversely to the y position, as already observed in figure 7. From this, the expression of $\Delta v_{||}$ as a function of the uncertainties in the two directions ($\mathrm{d}x$ and $\mathrm{d}y$) is:

$$\Delta v_{||} = \frac{E_z}{B_x} \left[\frac{\mathrm{d}x}{y} + \frac{x}{y^2} \mathrm{d}y \right] . \tag{17}$$

This yields two different expressions for the two screens:

$$\text{screen } xz\text{:} \;\; \Delta v_{||} = \frac{E}{BL_y} \left[\mathrm{d}x + \frac{x}{L_y} \mathrm{d}y \right] \tag{18}$$

with $\mathrm{d}x = \mathrm{d}x_\mathrm{d}$ and $\mathrm{d}y = \mathrm{d}y_a$, and

$$\text{screen } yz\text{:} \;\; \Delta v_{||} = \frac{EL_x}{B} \frac{\mathrm{d}y}{y^2} \tag{19}$$

with $\mathrm{d}y = \mathrm{d}y_a + \mathrm{d}y_d$.

The particles that land in the yz screen have travelled exactly the length of the device in the x direction ($\equiv L_x$), therefore there is no uncertainty $\mathrm{d}x$, and their position in y is affected by the detector width $\mathrm{d}y_\mathrm{d}$ and the aperture size $\mathrm{d}y_a$ (equation (19)). The ions impinging on the xz screen have travelled in the y direction L_y plus the uncertainty $\mathrm{d}y_a$, besides they are affected by $\mathrm{d}x_d$ in the x direction

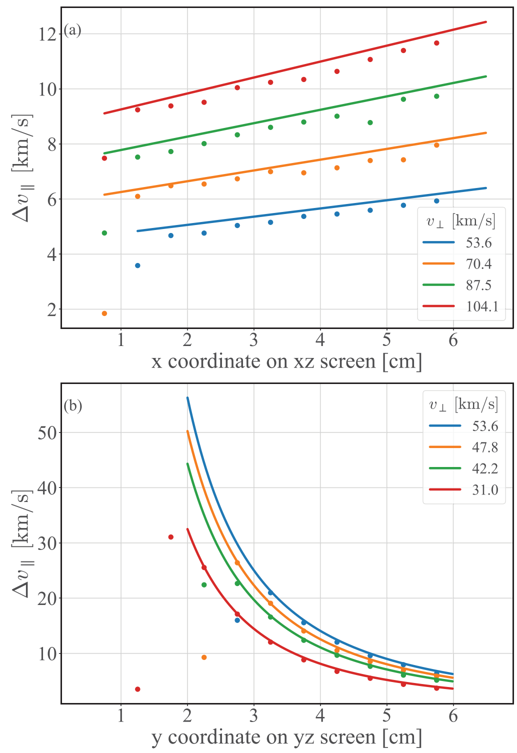

Figure 13. $\Delta v_{\parallel}$ as a function of the detector position along the screens. (a) linear relation between the position and $\Delta v_{\parallel}$ on the *xz* screen, for 4 fixed values of $v_{\perp}$. (b) inverse-square relation between the position and $\Delta v_{\parallel}$ on the *yz* screen, for other 4 fixed values of $v_{\perp}$. The simulated outputs (dots) agree with the analytic expressions (solid line, equations (18) and (19)).

(equation (18)). We compare equations (18) and (19) with the simulation results in figure 13 for the two screens and for 4 different values of $v_{\perp}$ each. For both screens, the analytic expression (solid line) and the simulated $\Delta v_{\parallel}$ (dotted) show good agreement. The data points that are out of the trend correspond to bins with few statistics, associated to the limited velocity range that is simulated, as discussed in section 4.2.2.

6. Calibration and evaluation of geometric factor

Once the particles are detected, we have to reconstruct the original VDF from the counts on the detectors. The general expression for the number of counts detected within a specific time interval as a function of the three parameters $(v_{\parallel}, v_{\perp}, \theta)$ is:

$$C\left(v_{\parallel}, v_{\perp}, \theta\right) \quad = \quad \iiiint v_{\perp}^{2}\, v_{\parallel}^{2}\, f\left(v_{\parallel}, v_{\perp}, \theta\right)\, \alpha\left(v_{\parallel}, v_{\perp}, \theta\right)\, dt\, \frac{\mathrm{d}v_{\parallel}}{v_{\parallel}}\, \frac{\mathrm{d}v_{\perp}}{v_{\perp}}\, d\theta \;, \tag{20}$$

where f is the distribution function and α is the transmission function, that takes into account the effective aperture area of the device. The full expression of $C(v_{\parallel}, v_{\perp}, \theta)$ is difficult to evaluate analytically as the integrals boundaries are coupled to each other, and simulations of the full 3D VDF would be required. A detailed comparison between the simulation results and this analytic expression is beyond the scope of this paper. Nevertheless the simulation outputs can be used to evaluate the integrated transmission function, that we define as the geometric factor (G) characteristic of the instrument [31, 54], and which is a key element for the reconstruction of the VDF.

α and G have to be estimated for each detector. The instrument returns the number of counts per detector for a given time interval. We can then convert this number to a VDF value for each detector, assuming that the VDF is constant over their velocity bandwidth. By considering the mean values of the perpendicular and parallel components, $v_{\perp}^{0}$ and $v_{\parallel}^{0}$, corresponding to each detector, we can construct the particle VDF in velocity space. We assume that the bins are small enough compared to the variations of the VDF, i.e. the device does not give any information on the shape of the distribution within each velocity bin, and its possible variations are not resolved. This approach might lead to errors if the distribution changes significantly over the acceptance ranges of the bins [54, 55]. Anyway, for the demonstration purposes of this paper we use this simplification, however future work will evaluate the associated error. Therefore, the number of detected ions in one detector during one acquisition can be written as:

$$C\left(v_{\|}^{0}, v_{\perp}^{0}, \theta^{0}\right) \quad \sim \quad v_{\perp}^{0^2}\, v_{\|}^{0^2}\, f\left(v_{\|}^{0}, v_{\perp}^{0}, \theta^{0}\right)\, \Delta t \iiint \alpha\left(v_{\|}, v_{\perp}, \theta\right) \frac{\mathrm{d}v_{\|}}{v_{\|}} \frac{\mathrm{d}v_{\perp}}{v_{\perp}}\, \mathrm{d}\theta, \tag{21}$$

where the limits of the integrals are the boundaries of parallel, perpendicular velocity, and phase detected in that detector. The transmission function integrated in the space of parameters associated to this detector is the effective G factor of the detector:

$$G\left(v_{\|}^{0}, v_{\perp}^{0}, \theta^{0}\right) = \iiint \alpha\left(v_{\|}, v_{\perp}, \theta\right) \frac{\mathrm{d}v_{\|}}{v_{\|}} \frac{\mathrm{d}v_{\perp}}{v_{\perp}}\, d\theta\,. \tag{22}$$

Thus, the relation that allows to convert the detected counts of one detector $C(v_{\|}^{0}, v_{\perp}^{0}, \theta^{0})$ to the VDF via the evaluated G factor is:

$$f\left(v_{\|}^{0}, v_{\perp}^{0}, \theta^{0}\right) \sim \frac{C\left(v_{\|}^{0}, v_{\perp}^{0}, \theta^{0}\right)}{G\left(v_{\|}^{0}, v_{\perp}^{0}, \theta^{0}\right)\, v_{\perp}^{0^2}\, v_{\|}^{0^2}\, \Delta t}\,. \tag{23}$$

This means that by computing the geometric factor for each detector, we calibrate the instrument: during operation, the experimental counts in the detectors are rescaled using the numerically computed G and the ion velocity distribution function is reconstructed.

The procedure to evaluate G of one selected detector is illustrated as an example. We run a simulation of a known flux of ions towards the device. The input parameters are: a known number of particles, uniformly distributed over a known area A_0, and over known ranges of the three parameters $D\theta, \frac{Dv_{\|}}{v_{\|}}, \frac{Dv_{\perp}}{v_{\perp}}$. The outputs of the simulation are: the number of particles detected on the detector and the detected range of parameters $\Delta\theta, \frac{\Delta v_{\|}}{v_{\|}}, \frac{\Delta v_{\perp}}{v_{\perp}}$. The detector is divided in sub-bins to look at the counts in the 3 parameters space within the detector. We build a 3D matrix that corresponds to the transmission function of the detector. Each element is computed as:

$$\alpha = \frac{c}{N} \cdot A_0 \cdot \left(D\theta \frac{Dv_{\|}}{v_{\|}} \frac{Dv_{\perp}}{v_{\perp}}\right) \cdot \left(\Delta\theta \frac{\Delta v_{\|}}{v_{\|}} \frac{\Delta v_{\perp}}{v_{\perp}}\right)^{-1}, \tag{24}$$

where c are the number of particles in the sub-pixel and N is the total number of simulated particles. The transmission function has the unit of an area: it can be considered as the effective aperture area of the detector. According to equations (22) and (24), the effective geometric factor is then given by:

$$G = \frac{C^0}{N} A_0\, D\theta \frac{Dv_{\|}}{v_{\|}} \frac{Dv_{\perp}}{v_{\perp}}\,, \tag{25}$$

where C^0 is the total number of particles reaching the detector.

Figure 14 shows three 2D representations of the transmission function α as a function of two parameters, integrating over the third one.

The counts are peaked at the mean values of the two components of the velocity, indicating a Gaussian transmission curve. Moreover, as expected, the majority of the ions are detected with a very small entrance gyro-phase θ, and the smaller is θ and the larger is the distribution of the counts in $v_{\perp}$. The demonstrated procedure must be repeated for each detector position and for each applied E field, in order to assess the full G factor and being able to reconstruct the entire distribution. The geometric factor depends on the ion mass and the magnetic field as well, as they have a role in the Larmor radius. This shows the importance of the simulations, as they are crucial to interpret the experimental results. For full calibration, it is required to simulate each experimental condition and to evaluate the associated G factor, allowing for the interpretation of the real velocity distribution functions.

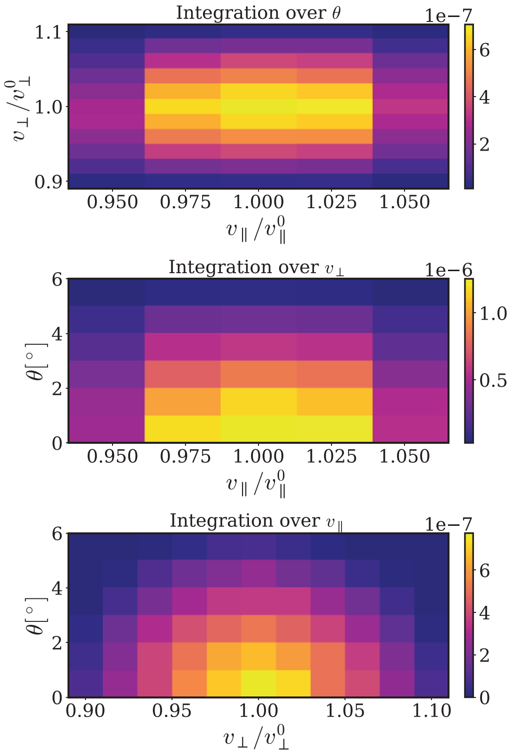

Figure 14. 2D representations of the transmission function $\alpha(v_\parallel, v_\perp, \theta)$.

6.1. Example of reconstruction of VDF

In order to prove the validity of the proposed calibration procedure, we now illustrate the reconstruction of a synthetic ion VDF.

We calculate the G factor for the case [gas = D_2, $B = 0.5$ T], applying the optimal values of the electric field as discussed in section 4.2.1. We build a synthetic Maxwellian distribution $f(v_\parallel, v_\perp)$, centred at $v_\parallel \simeq 69.2$ km s^{-1} and $v_\perp \simeq 53.6$ km s^{-1}. We then simulate particles distributed according this Maxwellian as they pass through our device. We evaluate the counts C that are detected in each detector for each applied electric field. Following the illustrated procedure, we remap the detected counts C into the reconstructed distribution f using equation (23). In figures 15(a) and (b), we compare the reconstructed VDF, in indigo, to the assumed input VDF in yellow, for the two components of the velocity. We show the detected counts in magenta. The count profile is rescaled through division by the denominator of equation (23). The resulting f correctly reproduces the original Maxwellian distribution.

To apply equation (23), we sum the contributions of the Gaussian transmission curves of each detector for the given velocity components. While for $v_\perp$ this method is straightforward—as the perpendicular component is fixed by the applied electric field —, in the case of $v_\parallel$ each data point corresponds to a different parallel velocity. Therefore, interpolation is required prior to the summation.

The small spurious dips in the reconstructed VDF in $v_\parallel$ (figure 15(a)) can be attributed to truncated detector transmission curves, as they register no counts for certain electric field values; consequently, some contributions are missing in the summation at specific data points. This effect is mitigated by the rescaling but still affects the reconstruction.

7. Summary and conclusions

The knowledge of the ion velocity distribution function is essential to study many plasma physics phenomena that influence the particle dynamics. Magnetic reconnection events and turbulence are two examples of universal plasma processes that strongly affect and depend on the particle distributions, both in laboratory and astrophysical environments. To this aim, we design a new diagnostic system, able to evaluate the ion velocity distribution function in velocity space. The proposed device, called DIVO, measures the VDF in $v_\perp$ and $v_\parallel$ by applying an electric field, perpendicular to the local magnetic field, that balances the force acting on the particles and breaks the gyration of magnetized ions. This scheme

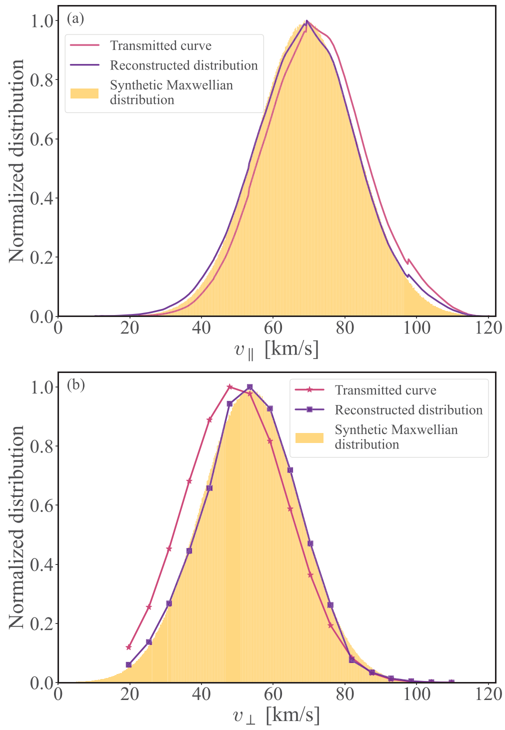

Figure 15. Reconstructed VDF as a function of $v_{\|}$ (a) and $v_{\perp}$ (b). The reconstructed distribution (indigo) is compared with the original synthetic Maxwellian VDF (yellow) and the detected counts (magenta).

resembles a Wien filter, but it is modified with a series of tight filtering plates that allow the selection of those ions that travel along a straight trajectory. These ions are then detected by spatially distributed detectors on the screens of the DIVO design. To our knowledge, this concept has not been applied before in the context of ion VDF measurements in fusion devices. If the distribution is gyrotropic, DIVO then analyses the distribution across the velocity components parallel and perpendicular to the magnetic field. The first one is evaluated from its relation with the impinging position of the ions on the detectors, while the perpendicular component of the velocity is estimated as the ratio between the applied electric field and the local magnetic field. We assess the expected resolution associated to these measurements with numerical simulations. The result shows that the parallel velocity resolution strongly depends on the size and number of detectors, with a different trend between the two detecting screens, and that the detectors parallel to the aperture are in general characterized by a better resolution. Assuming detectors of width of 0.5 cm, the expected parallel velocity resolution ranges between 6% for the most central detectors, and 40% for the ones nearest to the boundary of the device. The perpendicular velocities of the detected ions follow Gaussian transmission curves, all characterized by the same $V_{\perp}^{\mathrm{FWHM}}$, and therefore the associated resolution improves as the value of the velocity increases. The expected perpendicular velocity resolution is in the range between 4% and 37%, depending on the velocity, the local magnetic field and the charge-to-mass ratio of the ion. We also compare the results of the simulations with the analytic expressions that describe the motion of the ions inside the device as a function of the three parameters $v_{\|}, v_{\perp}, \theta$ and the associated uncertainties. We find a good agreement as the simulated quantities align with the analytic curves. Moreover, we illustrate the procedure to evaluate the geometric factor G of the device, necessary to calibrate the device and reconstruct the original distribution functions. We report the reconstruction of a simple synthetic Maxwellian input VDF as a proof of the validity of the proposed method.

The test particle simulations allow us to confirm the feasibility of the concept and to optimize a baseline design of the device. Future work will be devoted to new simulations dedicated to phenomena that have not been addressed in this study. These mainly include space-charge effects, the optimization of the modular scheme for the filtering of plasma electrons, the possible role of neutrals and impurities, and scattering of ions with other particles and the inner structure of the device. Once the conceptual design will be finalized, the second phase will include the analysis of thermo-mechanical stresses and the development of a first prototype of DIVO and its testing in relevant plasma conditions Finally, it is important to remark that, even though the design and simulations presented in this paper focus on

DIVO's application in the RFX-mod2 experiment, the proposed device can be adopted in different kinds of magnetized plasmas where ions have a gyro-radius of few mm or cm. In such environments, DIVO can be a useful instrument to complement the measurements of other diagnostics for the ion VDF.

Acknowledgments

We would like to thank F Auriemma and B Segalini for fruitful scientific discussions. This work was partially supported by the Royal Society (UK) and the Consiglio Nazionale delle Ricerche (Italy) through the International Exchanges Cost Share scheme/Joint Bilateral Agreement project 'Multi-scale electrostatic energisation of plasmas: comparison of collective processes in laboratory and space' (award Numbers IEC/R2/222050 and SAC.AD002.043.021). This work has been carried out within the framework of the EUROfusion Consortium, funded by the European Union via the Euratom Research and Training Programme (Grant Agreement No 101052200 — EUROfusion). This work has been carried out within the framework of Italian National Recovery and Resilience Plan (NRRP), funded by the European Union—NextGenerationEU (Mission 4, Component 2, Investment 3.1—Area ESFRI Energy—Call for tender No. 3264 of 28-12-2021 of Italian University and Research Ministry (MUR), Project ID IR0000007, MUR Concession Decree No. 243 del 04/08/2022, CUP B53C22003070006, 'NEFERTARI—New Equipment for Fusion Experimental Research and Technological Advancements with Rfx Infrastructure'). Views and opinions expressed are however those of the author(s) only and do not necessarily reflect those of the European Union or the European Commission. Neither the European Union nor the European Commission can be held responsible for them. This work was supported by STFC Consolidated Grant ST/W001004/1. This work has benefited from discussions during the International Space Science Institute (ISSI) Forum "Exploring the Synergies between Space and Laboratory Plasma Physics", held on 22-24 September 2025 in Bern, Switzerland.

Data availability statement

The data cannot be made publicly available upon publication because no suitable repository exists for hosting data in this field of study. The data that support the findings of this study are available upon reasonable request from the authors.

ORCID iDs

S Molisani 0009-0002-3457-5059
D Verscharen 0000-0002-0497-1096
M Zuin 0000-0002-0282-2978
D Abate 0000-0002-0331-3454
A Belpane 0009-0009-9054-1364
M Giacomin 0000-0003-2821-2008
O Pezzi 0000-0002-7638-1706
A Pimazzoni 0000-0003-2650-3944
I Predebon 0000-0002-2100-4698
F Pucci 0000-0002-5272-5404
L Sorriso-Valvo 0000-0002-5981-7758
N Vianello 0000-0003-4401-5346

References

[1] Yamada M, Kulsrud R and Ji H 2010 *Rev. Mod. Phys.* **82** 603–64
[2] Zweibel E G and Yamada M 2016 *Proc. R. Soc. A* **472** 20160479
[3] Horiuchi R 2018 *Plasma* **1** 68–77
[4] Burch J L and Nakamura R 2025 *Space. Sci. Rev.* **221** 19
[5] Priest E R 1998 *Astrophys. Space Sci.* **264** 77–100
[6] Longcope D W and Tarr L A 2015 *Philos. Trans. A* **373** 20140263
[7] Drake J F *et al* 2025 *Space. Sci. Rev.* **221** 27
[8] Paschmann G, Øieroset M and Phan T 2013 *Space. Sci. Rev.* **178** 385–417
[9] Wu Z *et al* 2023 *Astrophys. J.* **951** 98
[10] Bruno R and Carbone V 2005 *Living Rev. Sol. Phys.* **2** 4

[11] Sorriso-Valvo L *et al* 2019 *Phys. Rev. Lett.* **122** 035102
[12] Pezzi O, Blasi P and Matthaeus W H 2022 *Astrophys. J.* **928** 25
[13] Pezzi O *et al* 2024 *Astron. Astrophys.* **686** A116
[14] Drake J, Swisdak M, Che H and Shay M A 2006 *Nature* **443** 553–6
[15] Kowal G, de Gouveia Dal Pino E M and Lazarian A 2012 *Phys. Rev. Lett.* **108** 241102
[16] Chapman I T, Scannell R, Cooper W A, Graves J P, Hastie R J, Naylor G and Zocco A 2010 *Phys. Rev. Lett.* **105** 255002
[17] Wróblewski D and Snider R T 1993 *Phys. Rev. Lett.* **71** 859
[18] Igochine V 2023 *Phys. Plasmas* **30** 120502
[19] Marrelli L *et al* 2021 *Nucl. Fusion* **61** 023001
[20] Zuin M, Vianello N, Spolaore M, Antoni V, Bolzonella T, Cavazzana R, Martines E, Serianni G and Terranova D 2009 *Plasma Phys. Control. Fusion* **51** 035012
[21] Prager S C 1999 *Plasma Phys. Control. Fusion* **41** A129
[22] DuBois A M, Almagri A F, Anderson J K, Den Hartog D J, Lee J D and Sarff J S 2017 *Phys. Rev. Lett.* **118** 075001
[23] Magee R M *et al* 2011 *Phys. Rev. Lett.* **107** 065005
[24] Zuin M *et al* 2015 *42nd EPS Conf. on Plasma Physics*
[25] Fiksel G, Almagri A F, Chapman B E, Mirnov V V, Ren Y, Sarff J S and Terry P W 2009 *Phys. Rev. Lett.* **103** 145002
[26] Verscharen D 2025 In-situ measurements of space plasma: recent progress and future challenges *Plasma Phys. Contr. Fusion* submitted
[27] Pollock C *et al* 2016 *Space. Sci. Rev.* **199** 331–406
[28] Owen C J *et al* 2020 *Astron. Astrophys.* **642** A16
[29] Young D T *et al* 2004 *Space. Sci. Rev.* **114** 1–112
[30] Livi S *et al* 2023 *Astron. Astrophys.* **676** A36
[31] McComas D J *et al* 2017 *Space. Sci. Rev.* **213** 547–643
[32] Moseev D *et al* 2018 *Space. Sci. Rev.* **2** 7
[33] García-Muñoz M *et al* 2009 *Rev. Sci. Instrum.* **80** 053503
[34] Lazerson S A, Ellis R, Freeman C, Ilagan J, Wang T, Shao L, Allen N, Gates D and Neilson H 2019 *Rev. Sci. Instrum.* **90** 093504
[35] Korsholm S B 2022 *Rev. Sci. Instrum.* **93** 103539
[36] Bindslev h, Hoekzema J A, Egedal J, Fessey J A, Hughes T P and Machuzak J S 1999 *Phys. Rev. Lett.* **83** 3206
[37] Gobbin M *et al* 2022 *Nucl. Fusion* **62** 026030
[38] Huber A *et al* 2025 *High Power Laser Sci. Eng.* **13** e87
[39] Marrelli L *et al* 2019 *Nucl. Fusion* **59** 076027
[40] Carraro L *et al* 2024 *Nucl. Fusion* **64** 076032
[41] Lorenzini R *et al* 2009 *Nat. Phys.* **5** 570–4
[42] Bonomo F *et al* 2011 *Nucl. Fusion* **51** 123007
[43] Darling R B, Scheidemann A A, Bhat K N and Chen T-C 2002 *Sens. Actuators A: Phys.:Phys.* **95** 84–93
[44] Bower C A, Gilchrist K H, Lueck M R and Stoner B R 2007 *Sens. Actuators A: Phys.* **137** 296–301
[45] Refy D I *et al* 2019 *Rev. Sci. Instrum.* **90** 033501
[46] Langstaff D P 2002 *J. Mass Spectrom.* **215** 1–12
[47] Mathew A, Eijkel G B, Anthony I G M, Ellis S R and Heeren R M A 2022 *J. Mass Spectrom.* **57** e4820
[48] Fraser G W 2002 *J. Mass Spectrom.* **215** 13–30
[49] Agostinetti P *et al* 2026 Design and construction of a new fast reciprocating manipulator (FaRM) for RFX-mod2 *IEEE Trans. on Plasma Science* **54** 2562–68
[50] Boris J P 1970 *Proc.4th Conf. on Numerical Simulation of Plasmas*
[51] Qin H, Zhang S, Xiao J, Liu J, Sun Y and Tang W M 2013 *Phys. Plasmas* **20** 084503
[52] Birdsall C K and Langdon A B 2018 CRC Press
[53] Zenitani S and Umeda T 2018 *Phys. Plasmas* **25** 112110
[54] Nicolaou G , Ioannou C, Owen C J, Verscharen D, Fedorov A and Louarn P 2025 *Rev. Sci. Instrum.* **96** 075203
[55] Berger L *et al* 2025 *Astron. Astrophys.* **702** A135